Higgs dynamics in the early universe

Vis, J.M. van de

Chapter 6

Electroweak baryogenesis and the Standard Model Effective Field Theory

6.1 Introduction

The failure of the SM to produce the observed baryon asymmetry and the wish to connect baryogenesis to the EW scale have led to a large number of SM extensions that can lead to successful EWBG. Depending on the BSM details, such as the particle content and symmetries, different tests are required and each scenario requires a detailed phenomenological study. It would be a great advantage if the crucial aspects of all these models can be tested in a single framework. In principle, the SM Effective Field Theory (SM-EFT) could provide such a framework [242, 243, 277–282] as it provides a model-independent parametrization of BSM physics. The SM-EFT assumes that any BSM degrees of freedom are sufficiently heavy, such that they can be integrated out and that their low-energy effects can be captured by effective gauge-invariant operators containing just SM degrees of freedom. While an infinite number of effective operators exist, they can be organized by their dimension. The higher the dimension of the operators, the more suppressed their low-energy effects are by powers of E/Λ, where E is a typical low-energy scale, such as the electroweak scale, and Λ the scale of BSM physics. The first operators relevant for EWBG appear at dimension-six. If the SM-EFT is suitable for the description of EWBG, it would provide an attractive framework as the dimension-six operators have to a large extent been connected to low- and high-energy experiments already, while the EFT operators can be easily matched to specific UV-complete models. Pedagogical reviews of EFTs and the SM-EFT can be found for example in Refs. [283–287].

The applicability of the SM-EFT requires a perturbative expansion in E/Λ, which is potentially dangerous for EWBG applications. Extending the SM scalar potential with a dimension-six cubic interaction to ensure a strong first-order EWPT requires a relatively low scale $\Lambda \lesssim 800$ GeV [243], which can lead to a mismatch between calculations in the SM-EFT and specific UV-complete models, see for instance Ref. [280] for an analysis of the singlet-extended SM. Furthermore, EDM constraints on dimension-six CP-violating (CPV) operators potentially relevant for EWBG are typically in the multi-TeV range [288–291]. This difference in scale can be accommodated by assuming a different threshold for the CPV dimension-six operators such that $\Lambda_{\rm CP} > \Lambda$ [278]. In this way, it might be possible to use EFT techniques for the CPV sector despite the relatively low scale required for a strong first-order EWPT.

In this chapter we investigate a related issue of the EFT approach to EWBG. As mentioned, the EFT approach requires that the effects of higher-dimensional operators are suppressed with respect to the lower-dimensional ones. For energies around the electroweak scale and $\Lambda \simeq 800$ GeV, the expansion parameter $(E/\Lambda)^2$ seems at first sight to be sufficiently small for a perturbative expansion. In practice, the necessity of a first-order phase transition requires a fine balance between dimension-two, -four, and -six contributions to the Higgs potential. While no such balance is necessary for the CP-violating sector, successful EWBG requires an interplay of the scalar and CPV sectors, such that formally higher-order corrections to the latter might become relevant as well. To study this, we consider two specific EFTs which can be related via the classical equations of motion (EOMs). EOMs can be applied to EFTs to reduce the number of operators in the EFT basis [292]. Operators related via EOMs lead to identical observables up to higher-order corrections in the EFT expansion. That is, if the EFT is working satisfactory the two EFTs under investigation should lead to the same baryon asymmetry modulo small corrections. The main goal of our work is to perform a detailed test of this hypothesis.

A somewhat similar study was performed in Ref. [282], where it was concluded that the derivative operators in the EFT can no longer be eliminated by EOMs without explicitly specifying the dynamics of the phase transition. We improve on these results by carefully investigating — both analytically and numerically — the redundancy of the operators in the EFT, including important thermal effects. We also improve the EDM phenomenology with respect to Ref. [282], which neglected several relevant contributions.

Our study allows us to pin down where and how the EFT approach breaks down for the application of EWBG. We find that scenarios that are identical up to higher-order dimension-eight corrections lead to large differences in the baryon asymmetry. The breakdown of the EFT is not specific to the EWBG

calculation and in principle also arises at zero temperature where certain CPV interactions get $\mathcal{O}(1)$-corrections from dimension-eight operators. However, these interactions are largely unconstrained, and as far as the EDM phenomenology is concerned the scenarios that are related by the EOMs are equivalent. In the context of EWBG, however, we find that dimension-eight corrections strongly modify the strength of the CPV source term that drives the creation of the matter-antimatter asymmetry. While this modification is partially washed out due to SM processes that are active during the phase transition, it still leads to a reduction of the matter-antimatter asymmetry by a factor of order five. Higher-dimensional CPV operators can therefore not be neglected.

This chapter is organized as follows. In section 6.2 we introduce the SM-EFT operators we consider and how they are related via the EOMs. We also obtain the EDM constraints on the CPV operators. In section 6.3 we briefly discuss the parameters related to the EWPT. In section 6.4 we give the simplified set of transport equations relevant to our sources of CP violation. The baryon asymmetry is calculated in section 6.5. With the calculated asymmetries we test the impact of formally higher-order corrections, and identify the source for the breakdown of the EFT expansion. We summarize, conclude, and give an outlook in section 6.6. This chapter is based on Ref. [3], but some of the details have been left out. Whenever this is the case, we will refer to the relevant section of Ref. [3].

6.2 Effective scenarios for electroweak baryogenesis

We use the same notation for the SM Lagrangian as in eq. (1.4) [1]. We add a gluon term to the covariant derivative

$$D_\mu = \partial_\mu - ig_s G^a_\mu \frac{\lambda^a}{2} - igA^i_\mu \frac{\tau^i}{2} - ig' \frac{Y}{2} B_\mu \,, \tag{6.1}$$

where g_s is the $SU(3)_C$ coupling constant and $\lambda^a/2$ are the $SU(3)$ generators. The gluon field strength is

$$G^a_{\mu\nu} = \partial_\mu G^a_\nu - \partial_\nu G^a_\mu - g_s f^{abc} G^b_\mu G^c_\nu \,, \tag{6.2}$$

with f^{abc} the $SU(3)$ structure constant. The hypercharge assignments, Y, are 1/3, 4/3, $-2/3$, -1, -2, and 1 for Q_L, u_R, d_R, L_L, e_R, and Φ, respectively.

In eq. (1.4) we have suppressed fermion generation indices, but note that the Yukawa matrices are general 3×3 matrices in flavor space. We are mainly interested in interactions of the third generation

[1] Please note that we use a metric with different signature now. This leads to a sign change in the kinetic term.

of quarks. We neglect the Yukawa couplings to light fermions, but make an exception for the electron Yukawa which plays an important role when considering EDM constraints. We have left out the topological theta terms which play no role in our discussion.

The full set of dimension-six gauge-invariant operators was constructed in Ref. [293] and updated in Ref. [294]. There exist a large set of operators but only relatively few have impact on EWBG [279, 282]. Here, we consider two specific scenarios, which we label by scenario **A** and **B**, in which we consider a small subset of dimension-six operators:

A Here we extend the SM Lagrangian by two dimension-six operators

$$\mathcal{L}_6^{(A)} = -\kappa(\Phi^\dagger\Phi)^3 - \left[C_Y\,\bar{Q}_L y_t \tilde{\Phi}\, t_R\,(\Phi^\dagger\Phi) + \text{h.c.}\right], \tag{6.3}$$

where $\kappa \sim \Lambda^{-2}$ and $C_Y \sim \Lambda_{\text{CP}}^{-2}$ are couplings of the dimension-six operators. Q_L and y_t denote, respectively, the left-handed doublet of the third-generation quarks and the (33)-component of the up-type Yukawa-coupling matrix. As we have seen in section 5.2 the first term in eq. (6.3) modifies the scalar potential and can be used to ensure a strong first-order EWPT. The second term is a dimension-six modification of the top Yukawa coupling which causes a misalignment between the top-quark mass and the top-Higgs coupling such that the latter can obtain a physical CPV phase. In fact, for simplicity we consider a purely imaginary coupling $C_Y = i\tilde{c}_Y$, with $\tilde{c}_Y^* = \tilde{c}_Y$. This particular choice of dimension-six operators has been well studied [277, 278, 281, 282] and is sometimes called the minimal EWBG scenario [278].

B In this scenario we add the same modification to the scalar potential, but consider a different CPV structure. We use

$$\mathcal{L}_6^{(B)} = -\kappa(\Phi^\dagger\Phi)^3 - \alpha\left[C_{DD}\,\bar{Q}_L D^2\tilde{\Phi}\, t_R + C_{DD}\left(\bar{Q}_L^a t_R\right)\,\epsilon^{ab}\,\left(\bar{e}_L^b y_e e_R\right) + \text{h.c.}\right], \tag{6.4}$$

where e_L and y_e denote, respectively, the lepton doublet of the first generation and the real electron Yukawa coupling. α is a real constant introduced for normalization purposes. The second term provides the dimension-six CPV source for EWBG, while the third term describes a CPV top-electron coupling and is introduced for later convenience. As in scenario **A** we consider a purely imaginary coupling $C_{DD} = i\tilde{c}_{DD}$, with $\tilde{c}_{DD}^* = \tilde{c}_{DD}$.

It is possible to relate the two scenarios via the classical EOM for the scalar field [292]. From the Euler-Lagrange equations we obtain

$$(D^2\Phi^*)^a \;=\; -\mu^2(\Phi^*)^a - 2\lambda(\Phi^\dagger\Phi)(\Phi^*)^a - 3\kappa(\Phi^\dagger\Phi)^2(\Phi^*)^a + \epsilon^{ab}\bar{t}_R y_t Q_L^b - \bar{e}_L^a y_e e_R\,, \tag{6.5}$$

where we neglected the Yukawa couplings to other fermions and a term proportional to $\Lambda_{\rm CP}^{-2}$. Applying the EOM to eq. (6.4) shifts the Lagrangian into[2]

$$\mathcal{L}_6^{(B)} \to \mathcal{L}_6^{(\rm EOM)} = -\kappa(\Phi^\dagger\Phi)^3 + \alpha\left[\mu^2 C_{DD}\,\bar{Q}_L\,\tilde{\Phi}\,t_R + 2\lambda C_{DD}\,\bar{Q}_L\,\tilde{\Phi}\,t_R\,(\Phi^\dagger\Phi) + C_8O_8\right]\,, \tag{6.6}$$

where the top-electron term in eq. (6.4) has cancelled and the dimension-eight piece is given by

$$C_8O_8 = 3\,\kappa\,C_{DD}\,\bar{Q}_L\,\tilde{\Phi}\,t_R\,(\Phi^\dagger\Phi)^2\,, \tag{6.7}$$

which scales as $\sim \Lambda^{-2}\Lambda_{\rm CP}^{-2}$. If the EFT is working satisfactory this term should give rise to small corrections compared to the dimension-six terms in eq. (6.6). It is possible to simplify eq. (6.6) by redefining the Q_L and t_R in order to absorb the $\mu^2 C_{DD}$ term into the SM top-Yukawa coupling. The resulting Lagrangian then becomes

$$\mathcal{L}_6^{(\rm EOM)} = -\kappa(\Phi^\dagger\Phi)^3 + \alpha\left[2\lambda C_{DD}\,\bar{Q}_L\,\tilde{\Phi}\,t_R\,(\Phi^\dagger\Phi) + C_8O_8\right]\,, \tag{6.8}$$

which is of the same form as eq. (6.3) modulo the higher-order correction. For now, we will not remove the $\mu^2 C_{DD}$ piece and keep the form of eq. (6.6), mainly because it provides a cleaner relation between $\mathcal{L}_6^{(\rm EOM)}$ and the derivative of the scalar potential.

6.2.1 Zero-temperature phenomenology

We now discuss experimental constraints on the dimension-six Lagrangians. We begin with the Lagrangian in scenario **A**. We assume the scalar field picks up a vacuum expectation value $v_0 = 246$ GeV, and work in this section in the unitarity gauge $\Phi = (0,\, v_0 + h)^T/\sqrt{2}$, where h denotes the Higgs boson with zero-temperature mass $m_h \simeq 125$ GeV. Because of the modified scalar potential, in both scenarios the relations between the parameters μ^2 and λ on the one hand and v_0 and m_h^2 on

[2]Here we used that $C_{DD}\,(\bar{Q}_L t_R)(\bar{t}_R Q_L) + \text{h.c.} = 0$, for purely imaginary C_{DD}.

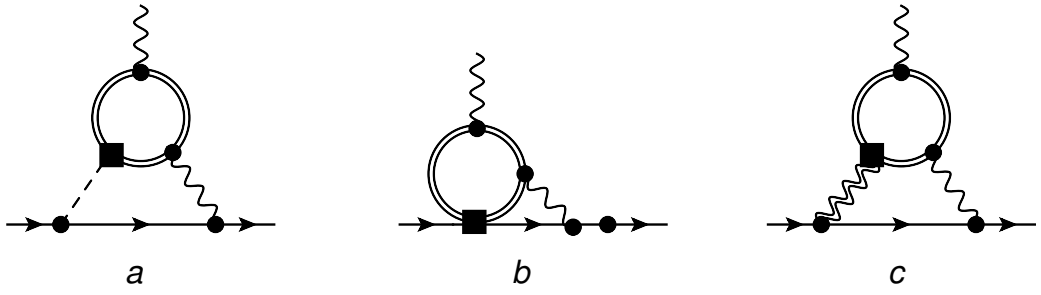

FIGURE 6.1: Two-loop diagrams contributing to the electron EDM. Single (double) lines denote the electrons (top quarks), dashed lines the Higgs boson, and wavy single (doubles) lines the photons (Z-bosons). Circles denote SM vertices, while squared denotes CPV dimension-six vertices. Only one topology for each diagram is shown.

the other, are modified by the κ term. At zero temperature we can express

$$\mu^2 = -\frac{1}{2}\left(m_h^2 - \frac{3}{2}\kappa v_0^4\right) , \qquad \lambda = \frac{1}{2}\left(\frac{m_h^2}{v_0^2} - 3\kappa v_0^2\right) . \tag{6.9}$$

Effects of the dimension-six κ interaction in particular induce deviations of the Higgs cubic and quartic interactions with respect to SM predictions. This manifests in processes such as double Higgs production, see e.g. Refs. [295, 296] for recent discussions. At the moment, such processes have not been accurately measured and current constraints on κ are weak.

In scenario **A**, the dimension-six term in eq. (6.3) gives a contribution to the top mass. We define the real top mass by [3]

$$m_t = \frac{v_0 y_t}{\sqrt{2}}\left(1 + \frac{v_0^2}{2} C_Y\right) . \tag{6.10}$$

Although this relation implies that y_t obtains a small imaginary part $\sim \mathcal{O}(\Lambda_{\rm CP}^{-2})$, this imaginary part only enters observables at $\mathcal{O}(\Lambda_{\rm CP}^{-4})$ which can be neglected. As such, from now on we use $y_t = \sqrt{2} m_t / v_0 \simeq 1$. The interactions between top quarks and Higgs bosons become

$$\begin{aligned} \mathcal{L}_h^{(\rm A)} &= -\frac{m_t}{v_0}\bar{t}_L t_R\, h - m_t C_Y\, \bar{t}_L t_R \left(v_0 h + \frac{3}{2}h^2 + \frac{1}{2}\frac{h^3}{v_0}\right) + \text{h.c.} \\ &= -\frac{m_t}{v_0}\bar{t}t\, h - m_t \tilde{c}_Y\, \bar{t}\, i\gamma^5 t \left(v_0 h + \frac{3}{2}h^2 + \frac{1}{2}\frac{h^3}{v_0}\right) . \end{aligned} \tag{6.11}$$

The top-Higgs interactions pick up a CPV component which can be probed in EDM experiments. In particular, the strongest constraint comes from the ACME experiment using the polar molecule

[3] Note that this definition differs from the m_t in the discussion above eqs. (5.18) and (5.19), where m_t denotes the finite temperature complex mass.

ThO, which sets a strong limit on the electron EDM[4] $d_e \leq 1.1 \times 10^{-29}\, e\,\text{cm}$ at 90% c.l. [297]. Please note that while Ref. [3], on which this chapter is based, was written, the most stringent bound was still $d_e \leq 8.7 \times 10^{-29}\, e\,\text{cm}$ at 90% c.l. [298]. In this chapter we have updated the results to the most recent constraint.

The dominant contribution to the electron EDM from the CPV top-Higgs couplings arises from the two-loop Barr-Zee diagram[5] in figure 6.1a [299] and is given by

$$\frac{d_e^{(\mathrm{A})}}{e} = -\frac{32 N_c}{9}\frac{\alpha_{em}}{(4\pi)^3} g(x_t)\, m_e\, \tilde{c}_Y\,, \tag{6.12}$$

in terms of the number of colors $N_c = 3$, the electron mass m_e, $x_t = (m_t/m_h)^2$, and the two-loop function

$$g(x_t) = \frac{x_t}{2}\int_0^1 dx\, \frac{1}{x(1-x)-x_t}\log\left(\frac{x(1-x)}{x_t}\right) \simeq 1.4\,. \tag{6.13}$$

The electron EDM limit then sets the strong constraint $|v_0^2 \tilde{c}_Y| < 0.001$. If we assume $|\tilde{c}_Y| = \Lambda_{\mathrm{CP}}^{-2}$, we obtain $\Lambda_{\mathrm{CP}} > 7.1$ TeV. In these expressions we have for simplicity neglected QCD renormalization-group effects that mildly affect the constraints for quarks [288, 289, 300].

In scenario **B**, the analysis is slightly more complicated. After electroweak symmetry breaking and assuming a purely imaginary C_{DD}, the CPV operators relevant for the EDM calculation become

$$\begin{aligned}
\mathcal{L}_h^{(\mathrm{B})} &= -\frac{\alpha \tilde{c}_{DD}}{\sqrt{2}}\,\bar{t} i\gamma^5 t\left(D^2 h + \frac{m_e}{v_0}\bar{e}e\right) - \frac{\alpha \tilde{c}_{DD}}{\sqrt{2}}\,\bar{t}t\,\bar{e} i\gamma^5 e \\
&= -\frac{\alpha \tilde{c}_{DD}}{\sqrt{2}}\,\bar{t} i\gamma^5 t\left(\partial^2 h + \frac{m_e}{v_0}\bar{e}e\right) - \frac{\alpha \tilde{c}_{DD}}{\sqrt{2}}\bar{t}t\left(M_Z \partial^\mu Z_\mu + \bar{e} i\gamma^5 e\right) + \dots\,,
\end{aligned} \tag{6.14}$$

in terms of the Z-boson mass, M_Z, and the dots denote interactions with two or more gauge bosons, which play no role in the EDM calculation. The last two terms in section 6.2.1 contribute to diagrams 6.1b and 6.1c and mutually cancel (this was the reason to include the CPV top-electron coupling in eq. (6.4)). The first two terms contribute to diagrams 6.1a and 6.1b. The contributions can be combined by using $k^2/(k^2 - m_h^2) = 1 + m_h^2/(k^2 - m_h^2)$ inside the loop, and together become

$$\frac{d_e^{(\mathrm{B})}}{e} = -\frac{32 N_c}{9}\frac{\alpha_{em}}{(4\pi)^3} g(x_t)\, m_e \left(-\tilde{c}_{DD}\frac{\alpha m_h^2}{\sqrt{2} v m_t}\right)\,, \tag{6.15}$$

[4]This limit assumes negligible contributions to the ThO observable from CPV semi-leptonic operators. This is justified in our scenarios as these semi-leptonic operators are only induced at loop level and strongly suppressed by small Yukawa couplings.

[5]We neglect diagrams where the internal photon is replaced by a Z-boson. These are suppressed by the electron-Z vector coupling $\sim (-1/4 + \sin^2\theta_W)$, where $\sin^2\theta_W \simeq 0.23$ is the square of the sine of the Weinberg angle.

which is of the same form as eq. (7.5), but with the replacement $\tilde{c}_Y \to -(\alpha m_h^2)/(\sqrt{2}v_0 m_t)\tilde{c}_{DD}$. By specifying α, we can ensure the same electron EDM predictions in the two scenarios. In what follows below, we will use

$$\alpha = -\frac{\sqrt{2}m_t v_0}{m_h^2}\,, \qquad \tilde{c}_Y = \tilde{c}_{DD} = \frac{1}{\Lambda_{\rm CP}^2}\,, \tag{6.16}$$

with the constraint $\Lambda_{\rm CP} > 7.1$ TeV from the limit on the electron EDM.

In section 6.2 we argued that scenario **A** and **B** are the same apart from higher-order corrections. So where are these higher-order corrections in the EDM calculation? To answer this question it is useful to look at eq. (6.6), which is the CPV Lagrangian after applying the EOM to scenario **B**. The physical real top mass is now given by

$$m_t = \frac{v_0}{\sqrt{2}}\left[y_t - \alpha C_{DD}\left(\mu^2 + \lambda v_0^2 + \frac{3}{4}\kappa v_0^4\right)\right] = \frac{v_0}{\sqrt{2}}\,y_t\,, \tag{6.17}$$

where the last equality follows from eq. (6.9). After setting α to its value in eq. (6.16), the interactions between top quarks and Higgs bosons become

$$\mathcal{L}_h^{(\rm EOM)} = -\frac{m_t}{v_0}\bar{t}t\,h - m_t\tilde{c}_{DD}\,\bar{t}\,i\gamma^5 t\left[v_0 h + \frac{3}{2}h^2\left(1 + \frac{2\kappa v_0^4}{m_h^2}\right) + \frac{1}{2}\frac{h^3}{v_0}\left(1 + \frac{12\kappa v_0^4}{m_h^2}\right)\right] + \cdots\,, \tag{6.18}$$

where the dots denote terms with four and five Higgs bosons. Comparing this to (6.11), we see that the dimension-eight corrections, $\sim \tilde{c}_{DD}\kappa$, only affect interactions with two or more Higgs bosons. These terms only contribute to the electron EDM at three loops and these contributions are therefore strongly suppressed. As such, as far the EDM phenomenology is concerned, scenarios **A** and **B** are essentially identical.

The CPV top-Higgs interactions give rise to the EDMs and chromo-EDMs of light quarks via very similar Barr-Zee diagrams. Another two-loop diagram involving a Higgs exchange inside a closed top-loop connected to external gluons, gives rise to a CPV three-gluon operator, the so-called Weinberg operator [301]. The quark (chromo-)EDMs and Weinberg operator in turn give rise to EDMs of the neutron and diamagnetic atoms such as ^{199}Hg and ^{225}Ra. With current experimental sensitivities, these limits are not competitive with the limit from the electron EDM. Furthermore, the hadronic and nuclear EDMs are sensitive to theoretical uncertainties due to hadronic and nuclear matrix elements. A much more detailed discussion can be found in Refs. [289, 302].

Finally, the CPV top-Higgs coupling can be directly probed in collider experiments, see e.g. Refs. [303–306]. However, for the foreseeable future, the resulting limits are significantly weaker than EDM constraints [302].

6.3 Bubble profile

Using the methods described in section 5.2.2 we determine a benchmark bubble profile φ_b, with parameters

$$\text{Benchmark}: \quad \kappa = 2\,\text{TeV}^{-2}, \quad T_N = 88\,\text{GeV}\,, \quad v_N = 144\,\text{GeV}, \quad v_w = 0.05\,, \tag{6.19}$$

that we will use to obtain the numerical results of section 6.5. The value for κ corresponds to a cutoff scale $\Lambda = 0.71\,\text{TeV}$ and we have checked that other values of κ consistent with a first-order EWPT lead to similar conclusions. Fitting to the kink solution (5.15), we estimate the width of the bubble wall to be $L_w T_N \simeq 9$. In vacuum the bubble wall would expand at the speed of light, but plasma interactions reduce the bubble wall velocity. The calculation of v_w is beyond the scope of this chapter, we will use the benchmark value given above [307–310].

Comparing the kink solution (5.15) and the full numerical solution, for scenario **A** we obtain a difference of only 10% in the baryon asymmetry. In scenario **B**, however, where the baryon asymmetry depends on the Laplacian of φ_b, the kink solution gives very different results. The reason is that the Laplacian contains a term $\frac{2}{\tilde{z}}\partial\varphi_b/\partial\tilde{z}$, which, when integrated over $\tilde{z}$, is only convergent because of the boundary conditions in eq. (5.10), which guarantee that $\partial\varphi_b/\partial\tilde{z}$ goes to zero at $\tilde{z} = 0$. The kink solution, however, does not satisfy the boundary condition exactly and consequently the integral diverges. The divergence may be tamed by a suitable regulator[6], but we will not follow this approach here. To avoid the divergence in scenario **B**, we will not apply the kink solution for the bubble profile, but instead use the numerical bounce solution in section 6.5.

6.4 Transport equations

All three Sakharov conditions needed for the creation of a matter-antimatter asymmetry are present in the two scenarios outlined in section 6.2. The first-order EWPT proceeds via the nucleation of bubbles of the new vacuum, which is an out-of-equilibrium process. The left- and right-handed top quarks in the plasma scatter off the bubble wall differently due to the CPV interactions in eqs. (6.3) and (6.4). As a result, a chiral asymmetry is built in front of the bubble wall. The SM sphaleron transitions only act on the left-handed particles, and transform the chiral asymmetry into a baryon asymmetry. The net baryon charge thus created is swept up by the expanding bubble, and

[6]For example, one can add an extra term to the kink solution in eq. (5.15) that is small in the bubble wall region, but cancels the divergency at the center $z = r_c$.

remains conserved provided the phase transition is strong enough such that sphaleron transitions are suppressed in the broken phase inside the bubble.

The expressions for the CPV-source and relaxation rate Γ_M are given in section 5.3. For our dimension-six operators, the $\mathscr{g}_t$-functions introduced in eq. (5.19) are given by

$$\begin{aligned}
\mathscr{g}_{t,A}(\varphi_b) &= y_t\varphi_b + \frac{iy_t\tilde{c}_Y}{2}\left[\frac{1}{2}T^2\varphi_b + \varphi_b^3\right], \\
\mathscr{g}_{t,B}(\varphi_b) &= y_t\varphi_b + i\alpha\tilde{c}_{DD}\left[\Box\varphi_b + \frac{T^2}{16}(3g^2 + g'^2 + 4y_t^2)\varphi_b\right], \\
\mathscr{g}_{t,\mathrm{EOM}}(\varphi_b) &= y_t\varphi_b - i\alpha\tilde{c}_{DD}\left[\left(\mu^2 + \frac{T^2}{2}\lambda\right)\varphi_b + \left(\lambda + \kappa T^2\right)\varphi_b^3 + \frac{3\kappa}{4}\varphi_b^5\right],
\end{aligned} \tag{6.20}$$

where the labels $i = \{A, B, \mathrm{EOM}\}$ correspond to the CPV operators in scenarios **A** (6.3), **B** (6.4), and **B** after applying the EOM (6.6). We should use eq. (6.9) to substitute for μ^2 and λ in $\mathscr{g}_{t,\mathrm{EOM}}(\varphi_b)$. Since we are in the rest frame of the bubble wall, the derivative operator $\Box$ reduces to the three-dimensional Laplace operator in spherical coordinates (with a minus sign due to the metric).

To compare the asymmetries produced in scenarios **A** and **B** in a consistent way it is important to work at the same order in perturbation theory in both the Higgs and the CPV sector. Thus we have neglected daisy diagram and have included the one-loop thermal corrections to the CPV interactions, which were calculated in Appendix A of Ref. [3].

In the two scenarios under investigation, the CPV resides in the top sector only[7]. Since leptons are only produced by small Yukawa couplings they are not taken into account. In addition, it is assumed that the second generation quarks and right-handed bottom are exclusively produced through strong sphaleron interactions, as is common in EWBG studies with a CPV top source [277, 281, 282] We will test these assumptions in chapter 7.

In addition to the assumptions in section 5.4 of gauge interactions and Higgs self-interactions in thermal equilibrium we now also drop the Yukawa rates and the Γ_M of the bottom and tau. The transport equations of the leptons completely decouple and the density of right-handed bottom quarks follows from eq. (5.31) and local baryon number conversation (5.37). In this approximation, the total chiral asymmetry is $n_L = 5q + 4t$ [311].

[7] We neglect the CPV top-electron coupling that appears in scenario **B** (see eq. (6.4)) as it is proportional to the small electron Yukawa coupling.

The full set of transport equations (5.32) reduces to [252]

$$\begin{aligned}\partial^\mu (t+q)_\mu &= -\Gamma_{ss}\left(\frac{2q}{k_q} - \frac{t}{k_t} + \frac{(q+t)}{k_{\text{eff}}}\right), \\ \partial^\mu h_\mu &= \Gamma_Y \left(\frac{t}{k_t} - \frac{h}{k_h} - \frac{q}{k_q}\right), \\ \partial^\mu (2t+q+h)_\mu &= -\Gamma_M \left(\frac{t}{k_t} - \frac{q}{k_q}\right) + S_R^{\not{CP}}.\end{aligned} \tag{6.21}$$

Γ_M and Γ_Y are proportional to $|\not{g}_{t,i}|^2 = (y_t\varphi_b)^2 + \mathcal{O}(\Lambda_{\text{CP}}^{-4})$. The difference between scenario **A** and **B** lies thus solely in the source term (5.27).

Furthermore we have

$$k_{\text{eff}} \equiv \left(\frac{4}{k_{q_{1L}}} + \frac{4}{k_{q_{2L}}} + \frac{1}{k_{u_R}} + \frac{1}{k_{c_R}} + \frac{1}{k_{d_R}} + \frac{1}{k_{s_R}} + \frac{1}{k_b}\right)^{-1}, \tag{6.22}$$

which is often approximated by $1/k_{\text{eff}} \simeq 9/k_b$ [311].

The set of transport equations (6.21) reduces to ordinary differential equations in the planar wall approximation of eq. (5.36), and can be solved to find the net chiral asymmetry $n_L = 5q + 4t$. We determine the baryon number density by integrating over the symmetric phase, using eq. (5.39).

6.5 The baryon asymmetry and investigation of the SM-EFT expansion

In this section we compare the baryon asymmetry computed in scenario **A** and **B**, and use this as guidance to investigate the validity of the SM-EFT expansion. We solve the transport equations (6.21) with the semi-analytic method outlined in Appendix B.2 of Ref. [3] (see also Ref. [312]). This method approximates all rates by a step function, and ignores the variation over the bubble-wall width. In addition, since the source peaks in the broken phase, it is set to zero in the symmetric phase. We feed the solution for $n_L(x)$ into eq. (5.39) to obtain the baryon asymmetry. We use the benchmark Higgs profile described by eq. (6.19).

6.5.1 Interaction strength and source term

The expressions for the $\mathscr{g}_{t,i}$ corresponding to our different CPV scenarios are given in eq. (6.20). The baryon asymmetry in particular depends on the combination $S^{\not{CP}} \propto \delta_i \equiv \mathrm{Im}(\mathscr{g}'_{t,i}\mathscr{g}^*_{t,i})$ which enters the source term, and varies between the scenarios.

In order for δ_i to be nonzero, we require that $\mathscr{g}_{t,i}$ has both real and imaginary parts, and $\mathscr{g}_{t,i}$ must have at least one term that depends non-linearly on the background field. For instance, for a linear dependence, $\mathscr{g}_{t,i} = c\,\varphi_b$ with c any complex number, it is clear that $\delta_i = \mathrm{Im}(|c|^2)\varphi_b\varphi'_b = 0$. The requirement of a non-linear dependence reflects that a CP-phase in the SM dimension-four Yukawa term can be rotated away and is not physical, see also the discussion surrounding eq. (6.8). With these considerations we obtain in the different scenarios

$$\delta_A = \tilde{c}_Y y_t^2 \varphi_b^3 \varphi'_b\,, \tag{6.23}$$

$$\delta_B = -\alpha y_t \tilde{c}_{DD} \left(\varphi_b \varphi_b^{'''} - \varphi_b^{'}\varphi_b^{''} + \frac{2}{z-r_c}\varphi_b\varphi_b^{''} - \frac{2}{z-r_c}\varphi_b^{'2} - \frac{2}{(z-r_c)^2}\varphi_b\varphi_b^{'} \right), \tag{6.24}$$

$$\delta_{\mathrm{EOM}} = -\alpha\, y_t \tilde{c}_{DD} \left[2\left(\frac{m_h^2 - 3v_0^4\kappa}{2v_0^2} + \kappa T^2 \right) \varphi_b^3 \varphi_b^{'} + 3\kappa \varphi_b^5 \varphi_b^{'} \right]. \tag{6.25}$$

The results for $\mathscr{g}_{t,\mathrm{EOM}}$ were obtained by first applying the EOM to the tree-level Lagrangian of scenario **B**, and then calculating the one-loop thermal corrections to $\mathscr{g}_{t,\mathrm{EOM}}$. It was checked in Appendix A.2 of Ref. [3] (where the $\mathscr{g}_{t,i}$ are denoted as f_i) that the same result is obtained if we first calculate the thermal corrections in scenario **B** to determine $\mathscr{g}_{t,B}$, and then apply the one-loop equations of motion to obtain $\mathscr{g}_{t,\mathrm{EOM}}$. Since the bounce solution φ_b is a solution of the one-loop equations of motion, see eq. (5.9), it follows that $\mathscr{g}_{t,\mathrm{EOM}} = \mathscr{g}_{t,B}$ and the source terms are equivalent — just as expected. This is somewhat obscured by the form of δ_i given above, but it is apparent from the $\mathscr{g}_{t,i}$-functions given in equation (A.18) of Ref. [3]. For this comparison, we stress that it is important to consistently include thermal corrections to the effective potential and to the CPV operators.

The difference between scenario **A** and **B** arises from the difference between δ_A and δ_{EOM}. Normalizing the CPV operators such that they give the same EDM constraints by using eq. (6.16), this gives the relation

$$\delta_B = \delta_{\mathrm{EOM}} = \delta_A \left(1 + \kappa \frac{v_0^2}{m_h^2} \left(3(\varphi_b^2 - v_0^2) + 2T^2 \right) \right). \tag{6.26}$$

The scenarios thus differ by the terms proportional to $\kappa\,\delta_A$ that scale as $\mathcal{O}(\Lambda^{-2}\Lambda_{\mathrm{CP}}^{-2})$.

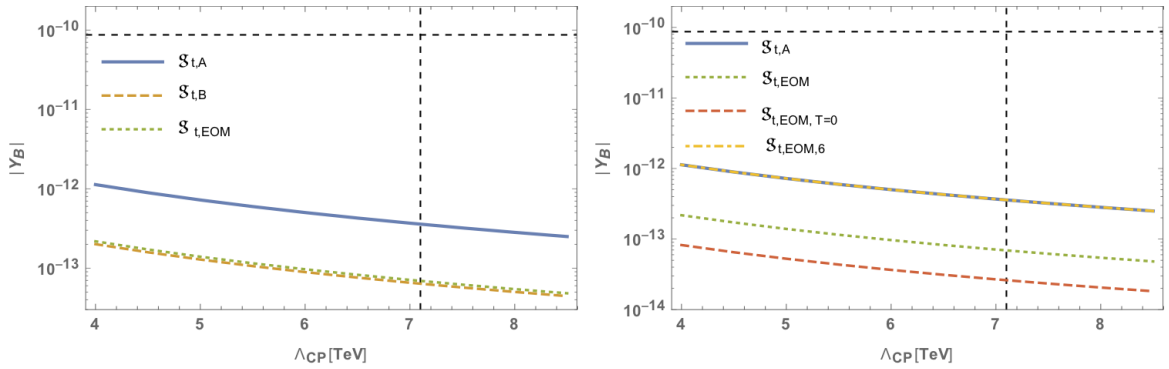

FIGURE 6.2: Absolute value of the baryon asymmetry for the considered dimension-six operators as a function of the effective CPV scale $\Lambda_{\rm CP}$. The vertical line indicates the experimental cutoff on $\Lambda_{\rm CP}$ and the horizontal line indicates the observed value of the baryon asymmetry.

6.5.2 Baryon asymmetry in scenario A and B

We will now discuss the baryon asymmetry in the two scenarios, starting with scenario **A**. We plot the baryon asymmetry as a function of $\Lambda_{\rm CP}$ in figure 6.2 in solid blue. The asymmetry measured by Planck is depicted by the dashed horizontal line, while the constraint on $\Lambda_{\rm CP}$ from EDM experiments ($\Lambda_{\rm CP} > 7.1$ TeV) is depicted by the vertical dashed line. Our results indicate that, given our approximation and input values, scenario **A** cannot produce the observed asymmetry for cutoff scales consistent with the EDM experiments. For the lowest allowed scale $\Lambda_{\rm CP} = 7.1$ TeV, corresponding to the most recent EDM constraint [297], the asymmetry is too small by roughly a factor 250.

The asymmetry in scenario **A** is much smaller than the observed value of Y_B. The computation should however be taken with a grain of salt. The baryon asymmetry is calculated using several approximations. For fermionic CPV sources in particular there are still a number of outstanding problems, see for example Refs. [226, 269]. Other issues are related to the accuracy of the vev-insertion approximation and the high-temperature expansion we applied in the calculation of the effective potential and the CPV source [313], and the uncertainty in the bubble wall velocity [307–309]. We therefore stress that our result for the baryon asymmetry suffers from significant theoretical uncertainties. An improvement of the formalism such that more accurate predictions can be made would of course be very relevant. But since the main goal of this chapter is to study the SM-EFT framework in the context of EWBG, we can live with these uncertainties as we are not too interested in the exact value of Y_B for now. Nevertheless, in chapter 7 we will investigate ways to enhance the value of the baryon asymmetry.

We now turn to scenario **B**. In this scenario the source is proportional to the much more complicated expression eq. (6.24) and depends also on the second and third derivative of the bubble profile. The

baryon asymmetry is obtained in the same way as in scenario **A** and is plotted in figure 6.2 in dashed yellow. The asymmetry is roughly five times smaller than in scenario **A** for the same values of $\Lambda_{\rm CP}$. The tension with EDM constraints is thus larger in scenario **B**.

Our results are obtained for the specific value of κ in eq. (6.19), which is expected to be representative for the narrow range in eq. (5.13) consistent with a first-order EWPT. We have checked that our results do not change qualitatively by small modifications of κ, but the exact difference between the value of the baryon asymmetry in scenarios **A** and **B** does depend on κ.

The large difference in the baryon asymmetry in the two scenarios points towards a breakdown of the SM-EFT expansion and indicates that the higher-order corrections in eq. (6.26) play an important role even though the power counting suggests that such effects are suppressed by $\mathcal{O}(v_N^2/\Lambda^2)$. In the next subsection we investigate the higher-order corrections in more detail.

6.5.3 Thermal corrections and dimension-eight effects

We study the difference between scenario **A** and **B** by dissecting $\delta_{\rm EOM}$ in eq. (6.25), which drives the CPV source after applying the EOM on scenario **B**. If we consider the complete $\delta_{\rm EOM}$, consisting of dimension-six and -eight (proportional to κ) contributions, we obtain the baryon asymmetry that is plotted in the left and right panel of figure 6.2 in dotted green. As it should, the asymmetry coincides with that of scenario **B**. The small differences of about 10% are due to numerical issues[8] related to the derivatives appearing in δ_B. The fact that the asymmetries agree provides a nontrivial check of our calculation.

If we now turn off dimension-eight contributions in $\delta_{\rm EOM}$, by setting $\kappa = 0$ in eq. (6.25), we reproduce the asymmetry in scenario **A**, as illustrated by the dotted-dashed yellow line in the right panel of figure 6.2. This is also expected as scenarios **A** and **B** are the same up to dimension-eight effects. The conclusion is that the formally higher-order terms in $\delta_{\rm EOM}$ proportional to $\sim \kappa\tilde{c}_{DD}$, reduce the obtained asymmetry by about a factor five and the EFT expansion explicitly fails. The dimension-eight terms can be separated into a temperature-independent and -dependent piece, and the dashed red line in the right panel of figure 6.2 is the result when we neglect the temperature-dependent piece of the CPV source. The difference with the full result is now roughly a factor 13 such that neglecting the temperature corrections to the CPV source is a poor approximation.

[8]The derivative terms in eq. (6.24) diverge in the limit $z \to r_c$ corresponding to the centre of the bubble, and the result is only finite once all terms are combined. Numerical errors arise if this cancellation is not perfect.

So what causes the breakdown of the EFT expansion? While the scale related to the $(\Phi^\dagger\Phi)^3$ term is not very high, $\Lambda = 0.71$ TeV, it is still significantly larger than any other scale, such as v_0, v_N, T_N, or particle masses, appearing in the computation. The problem is related to the demand of a strong first-order EWPT. The presence of a second minimum in the scalar potential requires a detailed balance between the dimension-two and -four terms in the SM Lagrangian and the $\kappa(\Phi^\dagger\Phi)^3$-term. This is the case for the zero-temperature potential as well as for the potential at the nucleation temperature T_N, but in the latter case the temperature corrections are included in the balancing act. This spoils the hierarchy between the dimension-four and -six terms in the effective potential, and thus after applying the EOMs for the Higgs field it spoils the hierarchy in the CPV sector.

This problem is not manifest in the EDM predictions in scenario **A** and **B**. The EDM constraints only depend on the linear top-Higgs coupling, which when expressed in terms of the physical masses, is the same in the two scenarios, and the higher-order terms (suppressed or not) are irrelevant. However, if we were able to accurately measure, for example, the CPV $h^2\,\bar{t}\,i\gamma^5\,t$-coupling, the two scenarios would give different predictions as can be seen by comparing eqs. (6.11) and (6.18); supposedly higher-order corrections in the EFT counting of the form $2\kappa v_0^4/m_h^2 \sim \mathcal{O}(1)$ give order-one corrections because of the balancing act in the Higgs potential.

The same breakdown of the EFT expansion occurs in the calculation of the baryon asymmetry. The difference between the obtained asymmetries in scenarios **A** and **B** arises from the dimension-eight terms in eq. (6.26). Figure 6.3 depicts the δ_{EOM} as a function of z. The green dotted line is the full result including all terms, the dashed red line ignores the temperature corrections, and the dotted-dashed yellow line ignores all dimension-eight effects and thus coincides with δ_A. The broken phase extends to $z \to \infty$, but φ_b' and consequently δ_i are only nonzero for $z < r_c \simeq 0.2\,\text{GeV}^{-1}$. The final baryon asymmetry depends on a weighted integral of the source over the broken phase[9].

The difference between the source with and without dimension-eight CPV interactions is not small at all. In fact, the peak value of δ_A is more than an order of magnitude larger than the peak value of δ_{EOM}. The right panel of figure 6.3 shows $\delta_{\text{EOM}}/\delta_A$ in the broken phase. The ratio goes from roughly -0.2 at $z = 0$ to 0.2 at $z = 0.2$. The difference mainly arises from zero-temperature contributions to δ_{EOM}, although the temperature corrections are non-negligible. Apart from the difference in overall scale, δ_{EOM} has a zero-crossing point which causes a partial cancellation between the positive and negative contributions in the integrand. The zero-crossing point emerges because the various terms in eq. (6.25) are of the same order and have opposite sign, which is related to the necessity of a

[9]See Appendix B.2 of Ref. [3] for more details on the solution to the transport equations. The source enters the solution through the β_i-parameters as given in eqs. (B.23) and (B.24).

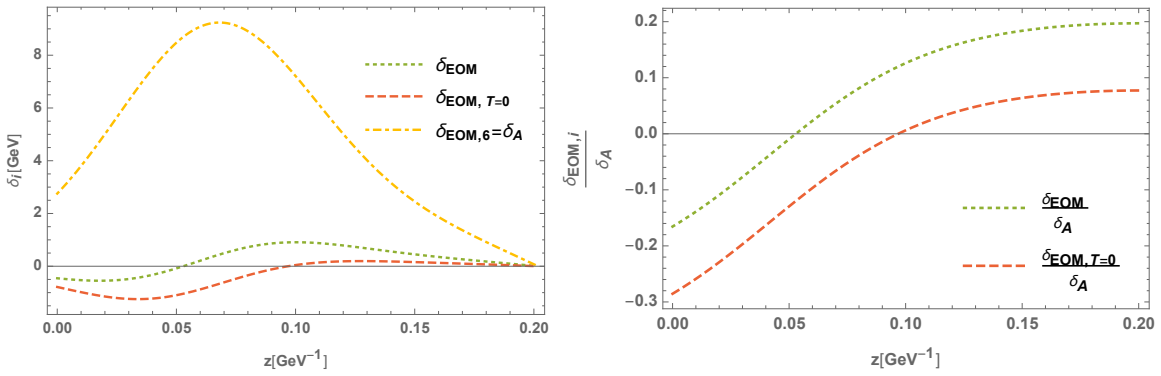

FIGURE 6.3: Left panel: $\delta_{\rm EOM}$ (green, dotted) and $\delta_{\rm EOM,6} = \delta_A$ (yellow, dotted-dashed) as a function of z in the broken phase. The difference arises from the terms proportional to $\kappa T^2\varphi_b^3$ and $\kappa\varphi_b^5$ in eq. (6.25). To see the relative importance of these two terms, we also plotted $\delta_{\rm EOM,\,T=0}$ (red, dashed), where the thermal corrections are neglected. Right panel: $\delta_{\rm EOM}/\delta_A$ in the broken phase. In dotted green the finite temperature corrections are included, in dashed red they are neglected.

second minimum in the potential. The cancellation is also present for $\delta_{\rm EOM,\,T=0}$, but occurs at a different value of z. On the other hand, δ_A is solely determined by the first term of eq. (6.25) and therefore has no cancellation between different contributions.

From figure 6.3 we can understand qualitatively why the asymmetry in scenario **B** is suppressed with respect to **A**. However, from the differences in the CPV source one would expect a larger difference in baryon asymmetry than the factor five we found and plotted in figure 6.2. Not only is the source in scenario **A** five to ten times larger over the whole range of relevant z-values, but there is also no zero-crossing and therefore no associated cancellation between different contributions. So what causes the relatively small difference in baryon asymmetry between scenarios **A** and **B** compared to the much larger difference in the CPV source?

The baryon asymmetry is produced as the electroweak sphaleron process converts the produced chiral asymmetry into a baryon asymmetry in the symmetric phase in front of the bubble wall. This chiral asymmetry n_L is calculated from the transport equations. In the symmetric phase the only non-zero rates on the r.h.s. of eq. (6.21) are the Yukawa and strong sphaleron interactions. Deep inside the symmetric phase these interactions are (approximately) in equilibrium, and consequently the combination of number densities

$$\left(\frac{2q}{k_q} - \frac{t}{k_t} + \frac{(q+t)}{k_{\rm eff}}\right) \simeq 0\,, \quad \left(\frac{t}{k_t} - \frac{h}{k_h} - \frac{q}{k_q}\right) \simeq 0\,, \qquad (z < z_{\rm eq})\,, \tag{6.27}$$

approximately vanish. Numerically, we find that this is an excellent approximation for $z_{\rm eq} \simeq -2\,{\rm GeV}^{-1}$. With these relations the chiral asymmetry can be written as $n_L = 5q + 4t = r_1 q$,

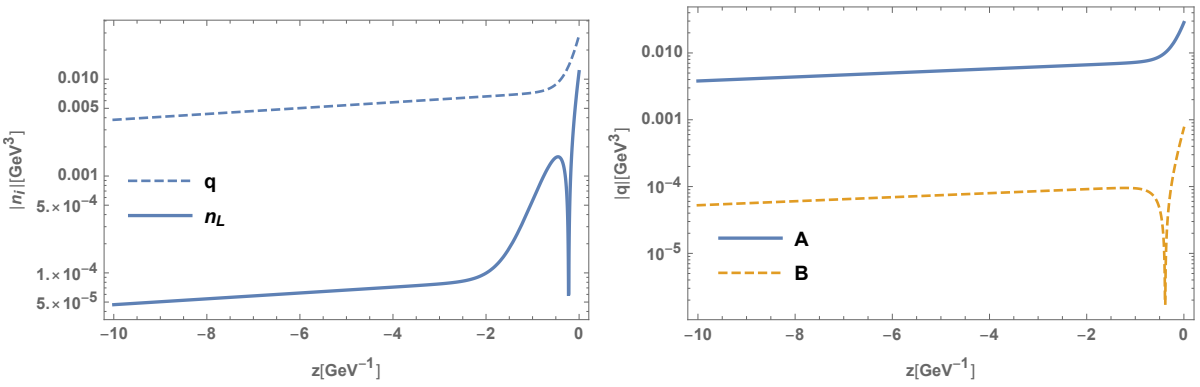

FIGURE 6.4: Left panel: absolute value of the number density q (dashed blue) and n_L (solid blue) in the symmetric phase for scenario **A**. The suppression of n_L is especially efficient for $z < -2\,\mathrm{GeV}^{-1}$. Right panel: absolute value of the number density q in the symmetric phase for scenario **A** (solid blue) and scenario **B** (dashed yellow). The density in scenario **A** is not only larger at the bubble wall at $z = 0$, but it has also diffused into the symmetric phase more effectively. The number densities t and h show similar behavior.

with

$$r_1 = 5 + \frac{4(2k_{\mathrm{eff}} + k_q)k_t}{k_q(k_{\mathrm{eff}} - k_t)}\,, \qquad (z < z_{\mathrm{eq}}). \tag{6.28}$$

The coefficient $r_1 = 0$ vanishes exactly in the massless limit, but also for our benchmark value it is small $r_1 \simeq -2 \times 10^{-2}$. The chiral asymmetry is thus much smaller than the individual number densities $n_L \ll h, q, t$, as was also noted in Refs. [314, 315].

The physical picture is as follows. The source term is non-zero inside the bubble and creates a chiral asymmetry, which then diffuses into the symmetric phase. However, on scales far away from the bubble $z < z_{\mathrm{eq}}$, the strong sphaleron and Yukawa transitions are in equilibrium and suppress the chiral asymmetry. This is shown in the left panel of figure 6.4, where the number density n_L is compared with q in scenario **A**. Electroweak sphaleron transitions transform the chiral asymmetry into a baryon asymmetry. However, this process is not efficient as only the small region right in front of the bubble $z_{\mathrm{eq}} < z < 0$ contributes significantly to the integral in eq. (5.39).

The above discussion is valid for both scenario **A** and **B**, which only differ by the source term that vanishes in the symmetric phase. It thus explains why in both scenarios baryogenesis is inefficient, and it is hard to obtain the observed asymmetry for cut-off scales consistent with EDM experiments. The difference, however, is that the source is much larger in scenario **A**. Consequently, the non-zero number densities diffuse into the symmetric phase more efficiently, as becomes clear from the right panel of figure 6.4, where the number density q is shown in the symmetric phase. If the cancellation in eq. (6.28) is not taken into account, and the chiral asymmetry would be estimated by $n_L \sim O(q)$

the obtained asymmetry would be much larger, as now the whole region $z < z_{\rm eq}$ contributes (and actually gives the dominant contribution).

The source in scenario **B** is much smaller, and consequently there is less diffusion of number densities into the symmetric phase. In effect, the number densities are peaked very close to the bubble wall and the wash-out of n_L due to the strong sphaleron and Yukawa interactions has a much smaller impact than for scenario **A**. This explains why the large difference in the CPV sources between scenarios **A** and **B** as shown in figure 6.3, are not completely transferred to large differences in the baryon asymmetry.

6.6 Discussion and conclusions

EWBG has been studied in many specific beyond-the-SM models. In this chapter, we have studied whether the crucial ingredients of EWBG can be studied without resorting to UV details of such models but instead by using effective operators to describe the EWPT and additional CP-violating sources. If applicable this would allow for a simple and model-independent description of a large class of models. Furthermore, specific SM extensions could be analyzed by matching to the EFT operators at the high-energy matching scale. As the SM-EFT operators can be and have been readily connected to low- and high-energy experiments this would allow for relatively easy tests of specific EWBG models. The main goal of this work was to study the effectiveness of the SM-EFT framework for EWBG.

The premise of the SM-EFT framework is that operators can be ordered by their dimension with higher-dimensional operators giving rise to suppressed contributions with respect to lower-dimensional ones. Based on this premise, it is possible to derive a minimal basis of operators at a given order in the EFT expansion, see for instance Refs. [293, 294], by applying EOMs. Certain operators are then redundant, up to higher-order corrections, and can be eliminated. In particular, the CPV operator in scenario **B** is usually removed from the basis. A full EFT analysis would then include all relevant dimension-six operators in a minimal basis. In this chapter we found that, for purposes of EWBG, the CPV operators in scenario **A** and **B** related by EOMs are not identical at all. The obtained baryon asymmetry differs by a large amount due to corrections from dimension-eight operators of the form

$$\mathcal{L}_8 = C_8\, \bar{Q}_L\, \tilde{\Phi}\, t_R\, (\Phi^\dagger \Phi)^2\,, \tag{6.29}$$

which therefore should be included in the analysis. In a general model-independent EFT approach there is then no, a priori, reason to not consider other dimension-eight operators that can contribute to the generation of the baryon asymmetry. The starting assumption of the SM-EFT approach is thus explicitly violated, and it is not possible to study EWBG and the related phenomenology in a fully model-independent way.

The breakdown of the effective field theory might be somewhat unexpected in view of the values of the scale of new physics required for successful baryogenesis. The scale corresponding to $\kappa = 2\,\text{TeV}^{-2}$ is $\Lambda = 0.71$ TeV while EDM experiments constrain $\Lambda_{\text{CP}} > 7.1$ TeV. There is no problem associated with the expansion in Λ_{CP}. While Λ is relatively low, it is still significantly larger than all other physical scales in the computation of the baryon asymmetry and a perturbative expansion might seem reasonable. However, in order for a first-order EWPT to occur, the $(\Phi^\dagger\Phi)^3$-term needs to strongly modify the scalar potential as the SM itself is not capable of providing such a phase transition. The parameters are thus chosen such that the dimension-four and the dimension-six terms at the minimum are approximately equal during the phase transition. We have calculated how this lack of hierarchy between dimension-four and -six contributions in the scalar sector is transferred to the CPV sector. We have shown that this leads to no problems for the low-energy EDM phenomenology which is, to a large extent, identical in the two scenarios. However, the CP-violating source which drives the generation of the baryon asymmetry is very different in the two scenarios leading to order-of-magnitude differences in particle number densities. Due to SM processes this large difference is not fully transferred to different baryon asymmetries, but nevertheless the total baryon asymmetry differs by a factor five in the two scenarios.

The difference in the baryon asymmetry raises the question whether EFT methods can still be useful for the study of EWBG. The breakdown of the EFT approach originates from the scalar sector, while the CPV sector is in principle better under control. One potential approach is then to consider a concrete UV-complete model for the phase transition, but keep the EFT approach for the CPV sector. For example, a modification of the Higgs sector that has been studied extensively in the literature [316–321] is the addition of a $\mathbb{Z}_2$-symmetric singlet S. A UV-completion has the advantage that there is no expansion in the problematic scale Λ, and the redundancy between the operators is maintained, but the price to pay is that the description of the electroweak phase transition is no longer model-independent. In addition, the EFT of the CPV sector needs to be extended to include effective operators that include the new singlet field. For a $\mathbb{Z}_2$-symmetric scenario, the first relevant operator is of the form $\mathcal{L} \sim \bar{Q}_L\tilde{\Phi}t_R|S|^2$ [322]. If the scalar field obtains a non-zero field value during the phase transition, these operators can give rise to a CPV phase contributing to EWBG that is

not significantly constrained by EDM experiments. The direct link between the baryon asymmetry and EDM experiments, which was present in the pure SM-EFT, is lost.

Another proposal, put forward in Ref. [282], is to work with the full set of dimension-six CPV operators, and to not use the EOMs to remove redundancies. In the context of this chapter, this means to treat the operators in scenario **A** and **B** as independent. Using a phenomenological description of the bubble wall in terms of a tanh-profile as in eq. (5.15), the Higgs sector can be specified by a few parameters, and thus kept generic. The disadvantage of this approach is that the physics leading to the phase transition can not be directly linked to collider experiments. Another problem is that the EDM or other low-energy experiments do not give constraints on the full set of dimension-six operators, since the redundancy is not broken at zero temperature such that observables only depend on a specific combination of operators that cannot be disentangled, even in principle. Finally, it is not clear how to match the EFT including redundant operators to a specific UV-complete model by an on-shell matching calculation at the high-energy scale.

In summary, we have investigated electroweak baryogenesis in the framework of the Standard Model EFT. We find that the EFT expansion breaks down due to the requirement of a strong first-order electroweak phase transition. We have shown that this also affects the expansion in the CP-violating sector of the EFT, such that higher-dimensional CP-violating operators cannot be a priori neglected. The pure Standard Model EFT is therefore not a suitable framework for electroweak baryogenesis. An extension of the EFT framework with additional scalar fields but effective CPV operators might be more suitable at the cost of losing model independence and a direct link to EDM phenomenology.